

# Event-based Convolutional Networks for Object Detection in Neuromorphic Cameras

Marco Cannici  
marco.cannici@mail.polimi.it

Politecnico di Milano  
Milano, Italy

Marco Ciccone  
marco.ciccone@polimi.it

Andrea Romanoni  
andrea.romanoni@polimi.it

Matteo Matteucci  
matteo.matteucci@polimi.it

## Abstract

Event-based cameras are bioinspired sensors able to perceive changes in the scene at high frequency with a low power consumption. Becoming available only very recently, a limited amount of work addresses object detection on these devices. In this paper we propose two neural networks architectures for object detection: YOLE, which integrates the events into frames and uses a frame-based model to process them; eFCN, a event-based fully convolutional network that uses a novel and general formalization of the convolutional and max pooling layers to exploit the sparsity of the camera events. We evaluated the algorithm with different extension of publicly available dataset, and on a novel custom dataset.

## Introduction

Fundamental techniques underlying Computer Vision base on the ability to extract meaningful features. To this extent, Convolutional Neural Networks (CNNs) rapidly became the first choice to develop computer vision applications such as image classification [9, 12, 62, 65], object detection [15, 30, 31], semantic scene labeling [16, 27, 66] and they have been recently extended also to non-euclidean domains such as manifolds and graphs [11, 19].

In most of the cases the input of these networks are RGB images. On the other hand, neuromorphic cameras [4, 26, 33] are becoming more and more widespread. These devices are bio-inspired vision sensors that attempt to emulate the functioning of biological retinas. As opposed to conventional cameras, which generate frames at a constant frame rate, these sensors output data only when a brightness change is detected. Whenever this happens, an event  $\mathbf{e} = \langle x, y, ts, p \rangle$  is generated indicating the position  $(x, y)$  and the instant  $ts$  at which the change has been detected and its polarity  $p \in \{0, 1\}$ , i.e., if the brightness change is positive or negative. The result is a sensor able to produce a stream of asynchronous events that sparsely encodes what happens inside the scene with microseconds resolution and with minimum requirements in terms of power consumption and bandwidth.

The growth in popularity of these type of sensors, and their advantages in terms of temporal resolution and reduced data redundancy, have led new algorithms and paradigms to fully exploit the advantages of event-based vision for varied applications, *e.g.*, features detection [21], visual odometry [20, 24] optical flow estimation [10]. The most popular method to deal with this kind of visual information are Spiking Neural Networks (SNNs) [17], a processing model aiming to improve the biological counterpart of artificial neural networks. The use of spikes as a mean of communication between neurons, however, limits the range of predictable values and prevents SNNs to be used to solve complex computer vision problems such as object detection. While in classification the use of spikes does not constitute a problem [23, 57] as label predictions can be obtained by looking at the output neuron that spikes first or more often, in object detection there is no obvious way of using a spike-based encoding to output bounding boxes information. Moreover, this type of communication makes SNNs not differentiable, making them difficult to train and use in complex scenarios.

An alternative solution to deal with event-based cameras is to make use of frame reconstruction procedures and conventional frame-based neural networks [25] which can instead rely on optimized training procedures. A recent solution proposed by Neil et al. [22], instead, makes use of LSTM cells to accumulate events over time and perform classification.

Even if event-cameras are becoming increasingly popular, due to their relative novelty, only very few datasets for object detection in event-based data streams are available. As a result, a limited number of object detection algorithms have indeed been proposed in literature [9, 14, 28]. In this paper we present a hybrid approach to feature extraction in neuromorphic cameras. Our framework allows the design of object detection networks able to exploit events and sparsely recompute features while still preserving the advantages of conventional neural networks. The key contributions of this paper are:

1. A frame integration procedure inspired by SNNs which encodes the timing of the events in the intensity of each pixel (Section 2).
2. A basic model for object detection in neuromorphic cameras that integrates events (Section 2).
3. The formalization of event-based convolutional and max-pooling layers used to define fully-convolutional neural networks for event-based object detection (Section 3).
4. A set of novel datasets to test object detection with event cameras (Section 4).

## 2 YOLE: You Only Look Events

In this section we describe an approach to adapt conventional frame-based neural networks to deal with event-based inputs. Sparse events generated by the neuromorphic camera are integrated into a *volatile frame*, a spatial structure to maintain events information through time. After this frame has been reconstructed, a general neural network can be applied as with classical images.

**Leaky Integrator.** The design of the proposed frame integration mechanism takes inspiration from the functioning of Spiking Neural Networks (SNNs) to maintain memory of past events. Every time an event with coordinates  $(x_e, y_e)$  with timestamp  $ts_t$  is received, the corresponding pixel of the integrated frame is incremented of a fixed amount  $\Delta_{incr}$ . At the same time, the whole frame is decremented of a quantity that depends on the time elapsed between

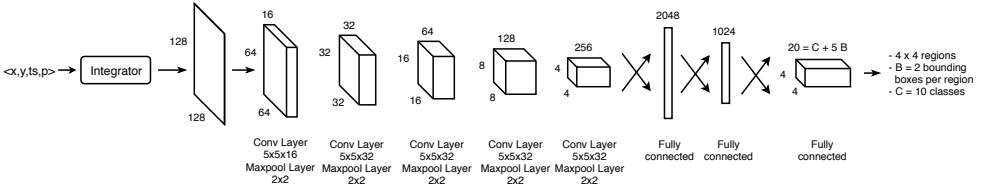


Figure 1: The YOLE detection network based on YOLO. The input frames are divided into a grid of  $4 \times 4$  regions which predict 2 bounding boxes each.

the last received event and the previous one. The described procedure can be formalized by the following relations:

$$p_{x_m, y_m}^t = \begin{cases} \max(p_{x_m, y_m}^{t-1} - \lambda \cdot \Delta_{ts}, 0) + \Delta_{incr} & \text{if } (x_m, y_m)^t = (x_e, y_e)^t \\ \max(p_{x_m, y_m}^{t-1} - \lambda \cdot \Delta_{ts}, 0) & \text{otherwise} \end{cases}, \quad (1)$$

where  $p_{x_m, y_m}^t$  is the value of the pixel in position  $(x_m, y_m)$  of the integrated frame and  $\Delta_{ts} = t_s^t - t_s^{t-1}$ .  $\lambda$  and  $\Delta_{incr}$  are correlated:  $\Delta_{incr}$  determines how much information is contained in each single event whereas  $\lambda$  defines the decrement of information in time. Given a certain choice of these parameters, similar frames can be obtained by using, for instance, a higher increment  $\Delta_{incr}$  and a higher temporal  $\lambda$ . For this reason, we fix  $\Delta_{incr} = 1$  and we vary only the  $\lambda$  one based on the dataset to be processed. Pixel values are prevented to become negative by means of the max operation.

Other frame reconstruction procedures, such as the one in [25] divide the time in constant and predefined intervals. Frames are obtained by setting each pixel to a binary value (depending on the polarity) if at least an event has been received within the reconstruction interval. With this mechanism however, time resolution is lost and the same importance is given to each event, even if it is noise. The proposed method, instead, does not distinguish the polarity of the events, obtaining frames invariant to the object movement, and performs continuous and incremental integration, characteristics that allowed us to develop the event-based framework presented in Section 3.

**Event-based Object Detection.** We identified YOLO [60] as a good candidate for object detection to be used in our event-based framework: it is fully-differentiable and it is able of producing predictions with small input-output delays. By means of a standard CNN and with a single run of the model, it is able to simultaneously predict not only the class, but also the position and dimension of every object present inside the scene. We used the YOLO training mechanism and the previous frame integration procedure to train our YOLE model. Its architecture is depicted in Figure 1. Note that in this context, we use the term YOLO to refer only to the training procedure proposed by Redmon et al. [60] and not to the specific network architecture. We used indeed a simpler structure for our models as explained in Section 4. Nevertheless, YOLE did not exploit the sparse nature of events; thus, in the next section, we propose a fully event-based framework for convolutional networks.

### 3 Event-based Fully Convolutional Networks (eFCN)

Conventional CNNs for video analysis usually treat every frame independently and recompute all the feature maps entirely, even if consecutive frames differ from each other only in small portions. Beside being a significant waste of power and computations, this approach

does not match the nature of event-based cameras which directly output the location where the changes happen.

To exploit the event nature of neuromorphic vision, we propose a modification of the forward pass of fully convolutional architectures. In the following the convolution and pooling operations are reformulated to produce the final prediction by recomputing only the features in correspondence of the regions affected by the events. Feature maps maintain their state over time and are updated only as a consequence of incoming events. At the same time, the leaking mechanism that allows past information to be forgotten acts independently on each layer of the CNN and enables features computed in the past to fade away as their visual information starts to disappear in the volatile frame.

This method can be applied to any convolutional architecture. Indeed, a CNN trained to process frames reconstructed from streams of events can be easily converted into an event-based CNN without any modification on its layers composition and by using the same weights learned while observing frames maintaining its output unchanged.

### 3.1 Volatile Frame Reconstruction Layer

The *volatile frame reconstruction layer* extends the method presented in Section 2 to recover the integrated frame so that sequences of multiple events can be processed at the same time. Every pixel that corresponds to an event coordinate is incremented by  $\Delta_{incr}$  and the leaking mechanism is applied on the whole frame by using the timestamp  $ts_{last}$  of the most recent event in the sequence. All the pixels are decremented by the same negative quantity  $\Delta_{leak} = -(ts_{last} - ts_{prev}) \cdot \lambda$  which is summed up to their previous value.

To allow subsequent layers to locate changes in reconstructed frames, the frame integration layer performs also the following set of operations: (i) it sends the list of incoming events to the next layer so that modified pixels can be updated. (ii) it communicates the decrement  $\Delta_{leak}$  to all the subsequent layers to update feature maps in correspondence of regions not affected by any event. (iii) it communicates which pixels have been reset to 0 to prevent their value becoming negative (max operator in Equation (1)).

### 3.2 Event-based Convolutional Layer

The *event-based convolutional* (e-conv) layer proposed uses events to determine where the input feature map has changed with respect to the previous time step and, therefore, which parts of its *internal state*, i.e., the feature map computed at the previous time step, must be recomputed and which parts can be reused. As opposed to the frame reconstruction layer, the update mechanism that allows past information to leak away over time does not only depend on the time elapsed from the last time the state was updated. Indeed, the transformations applied by previous layers and the composition of their activation functions may cause  $\Delta_{leak}$  to act differently in different parts of the feature map. We face this issue by storing an additional set of information and by using a particular class of activation functions for the hidden layers of the network.

Let's consider the first layer of a CNN which processes the frames reconstructed by the frame integration layer and which computes the convolution of a set of filters  $W$  with bias  $b$  and activation function  $g(\cdot)$ . The computation performed on each receptive field is:

$$y_{ij(1)}^t = g \left( \sum_h \sum_k x_{hk}^t W_{hk(1)} + b_{(1)} \right) = g(\tilde{y}_{ij(1)}^t), \quad (2)$$

where  $h, k$  select a pixel  $x'_{hk}$  of the current receptive field at time  $t$  and its corresponding value in the kernel  $W$ , while the indices  $i, j$  indicate the location in the output feature map.

When a new event arrives, the frame reconstruction layer decreases all the pixels by  $\Delta_{leak}$ , *i.e.*, a pixel not directly affected by the event becomes:  $x'_{hk}{}^{t+1} = x'_{hk}{}^t + \Delta_{leak}^{t+1}$ , with  $\Delta_{leak}^{t+1} < 0$ .

At time  $t + 1$  Equation (2) becomes:

$$y_{ij(1)}^{t+1} = g \left( \sum_h \sum_k (x'_{hk} + \Delta_{leak}^{t+1}) W_{hk(1)} + b_{(1)} \right) = g \left( \tilde{y}_{ij(1)}^t + \Delta_{leak}^{t+1} \sum_h \sum_k W_{hk(1)} \right). \quad (3)$$

If  $g(\cdot)$  is a piecewise linear activation function, as ReLU or Leaky ReLU, and we assume that the updated value will not cause the activation function to change the sign of the output with respect to the input, Equation 3 can be rewritten as follows:

$$y_{ij(1)}^{t+1} = y_{ij(1)}^t + \Delta_{leak}^{t+1} \alpha_{ij(1)} \sum_h \sum_k W_{hk(1)}, \quad (4)$$

where  $\alpha_{ij(1)}$  is the coefficient applied by the piecewise function  $g(\cdot)$  which depends on the feature value in position  $(i, j)$ . When the previous assumption is not satisfied, the feature is recalculated like its receptive field was affected by an event.

Consider now a second convolutional layer attached to the first one:

$$\begin{aligned} y_{ij(2)}^{t+1} &= g \left( \sum_h \sum_k \left( y_{hk(1)}^t + \Delta_{leak}^{t+1} \alpha_{hk(1)} \sum_{h'} \sum_{k'} W_{h'k'(1)} \right) W_{hk(2)} + b_{(2)} \right) \\ &= y_{ij(2)}^t + \Delta_{leak}^{t+1} \alpha_{ij(2)} \sum_h \sum_k \left( \alpha_{hk(1)} \sum_{h'} \sum_{k'} W_{h'k'(1)} \right) W_{hk(2)} \\ &= y_{ij(2)}^t + \Delta_{leak}^{t+1} \alpha_{ij(2)} \sum_h \sum_k F_{hk(1)} W_{hk(2)} = y_{ij(2)}^t + \Delta_{leak}^{t+1} F_{ij(2)}. \end{aligned} \quad (5)$$

The equation can be easily extended by induction as follows:

$$y_{ij(n)}^{t+1} = y_{ij(n)}^t + \Delta_{leak}^{t+1} F_{ij(n)}, \quad \text{with} \quad F_{ij(n)} = \alpha_{ij(n)} \sum_h \sum_k F_{hk(n-1)} W_{hk(n)}. \quad (6)$$

where  $F_{hk(n)}$  expresses how visual inputs are transformed by the network in every receptive field  $(h, k)$ .

The max operator applied by the frame integration layer can be interpreted as a ReLU, and Equation (4) becomes:

$$y_{ij(1)}^{t+1} = y_{ij(1)}^t + \Delta_{leak}^{t+1} \alpha_{ij(1)} \sum_h \sum_k F_{hk(0)} W_{hk(1)} \quad (7)$$

where the value  $F_{hk(0)}$  is 0 if  $(h, k)$  is negative and 1 if it is positive. Notice that  $F_{hk(n)}$  needs to be updated only when the corresponding feature changes enough to make the activation function use a different coefficient  $\alpha$ , *e.g.*, from 0 to 1 in case of ReLU. Events are used to communicate the change to subsequent layers so that also their update matrix can be updated accordingly.

The internal state of the e-conv layer, therefore, comprises the feature maps  $y_{(n)}^{t-1}$  and the update values  $F_{(n)}^{t-1}$  computed at the previous time step. The initial values of the internal state are computed making full frame inference on a blank frame; this is the only time the network needs to be executed entirely. As a new sequence of events arrives the following operations are performed (see Figure 2(a)):

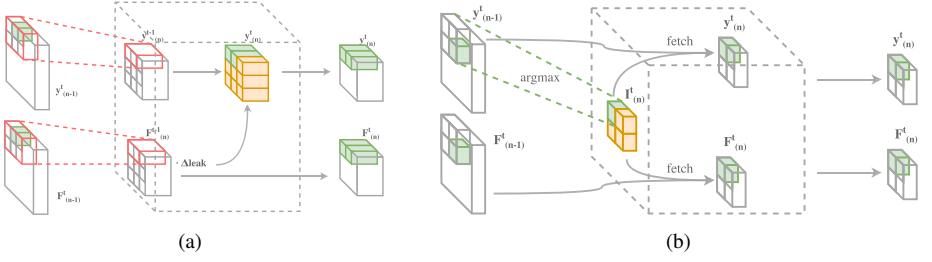


Figure 2: The core structure of the e-conv (a) and e-max-pooling layers (b). The internal states and the update matrices are recomputed locally only in correspondence of the events (green cells) whereas the remaining regions (depicted in yellow), are obtained reusing the previous state.

- i. Update  $F^{t(n)-1}$  locally on the coordinates specified by the list of incoming events (Eq. (6)).
- ii. Update the feature map  $y_{(n)}$  with Eq. (7) in the locations which are not affected by any event and generate an output event where the activation function coefficient changed.
- iii. Recompute  $y_{(n)}$  through Equation (2) in correspondence of the incoming events and output which receptive field has been affected.
- iv. Forward the feature map and the events generated in the current step to the next layer.

### 3.3 Event-based Max Pooling Layer

The location of the maximum value in each receptive field of a max-pooling layer is likely to remain the same over time. An event-based pooling layer, hence, can exploit this property to avoid recomputing every time the position of maximum values.

The internal state of an event-based max-pooling (e-max-pool) layer can be described by a *positional matrix*  $I_{(n)}^t$ , which has the shape of the output feature map produced by the layer, and which stores, for every receptive field, the position of its maximum value. Every time a sequence of events arrives, the internal state  $I_{(n)}^t$  is updated by recomputing the position of the maximum values in every receptive field affected by an incoming event. Then the internal state is used both to build the output feature map and to produce the *update matrix*  $F_{(n)}^t$  by fetching the previous layer on the locations provided by the indices  $I_{ij(n)}^t$ . For each e-max-pool layer, the indices of the receptive fields where the maximum value changes are communicated to the subsequent layers so that the internal states can be updated accordingly. This mechanism is depicted in Figure 2(b).

Notice that the leaking mechanism acts differently in distinct regions of the input space. Features inside the same receptive field can indeed decrease over time with different speeds as their update values  $F_{ij(n)}^t$  could be different. Therefore, even if no event has been detected inside its region, the position of the maximum value might change and, in principle, the update procedure has to check if the maximum value has changed both in the receptive fields affected by an event and in the remaining regions. However, if an input feature  $M$  corresponds to the maximum value of a receptive field  $R$  and has also the minimum update rate  $F_{M(n-1)}$  among the input features in  $R$ , the output feature will decrease slower than all the others and its value will remain the maximum. In this case, we do not need to recompute the maximum until a new event arrives at this receptive field.

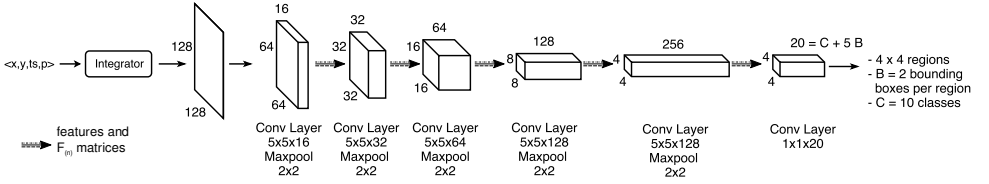


Figure 3: Fully-convolutional detection network based on YOLE. The first 5 convolutional layers extract a hierarchy of abstract representations. The last layer is used to map the feature vectors into a set of 20 values which define the parameters of the predicted bounding boxes.

### 3.4 Event-based Fully Convolutional Object Detection

To fully exploit the event-based layers presented so far, YOLE needs to be converted to a fully convolutional object detection network replacing all its layers with their event-based versions (see Figure 3). Moreover, fully-connected layers are replaced with  $1 \times 1$  e-conv layers that map features extracted by the previous layers into a precise set of values defining the bounding boxes parameters predicted by the network.

This architecture divides the  $128 \times 128$  field of view into a grid of  $4 \times 4$  regions that predicts 2 bounding boxes each and classify the detected objects into 10 different classes. Each one of the  $32 \times 32$  regions in which the frame is divided is processed independently. The last  $1 \times 1$  e-conv layer is used to decrease the dimensionality of the feature vectors and to map them into the right set of parameters, regardless of their position in the field of view.

## 4 Experiments

**Datasets.** Only few event-based object detection datasets are publicly available in the literature: N-MNIST [24], MNIST-DVS [63] and N-Caltech101 [24]. These datasets are obtained from the original MNIST [13] and Caltech101 [0] datasets by recording the original images with an event camera while moving the camera itself or the images in the datasets. We performed experiments on N-Caltech101 and on two enhanced versions of N-MNIST and MNIST-DVS, i.e., *Shifted N-MNIST* and *Shifted MNIST-DVS*, with the purpose of better testing the translation-invariance of detection models. Moreover we present a novel dataset, named *Blackboard MNIST*, and an extension of *POKER-DVS* [63], an event-based dataset originally designed for object tracking. See the supplementary materials for further details<sup>1</sup>.

**Experiments Setup.** Event-based datasets are generally simpler than the RGB ones used in the original YOLO paper. Therefore, we designed the object detection networks taking inspiration from the simpler LeNet [13] model with 6 conv-pool layers for feature extraction. Both YOLE and eFCN share the same structure up to the last regression/classification layers.

For what concerns the N-Caltech101 dataset, we used a slightly different architecture inspired by the structure of the VGG16 model [54]. The network is composed by only one layer for each group of convolutional layers, as we noticed that a simpler architecture achieved better results. Moreover, the dimensions of the last fully-connected layers have been adjusted such that the frame is divided into a grid of  $5 \times 7$  regions predicting  $B = 2$  bounding boxes each. As in the original YOLO architecture we used for all models Leaky ReLU for the activation functions of hidden layers and a linear activation for the last one.

<sup>1</sup>Shifted N-MNIST, Shifted MNIST-DVS, POKER-DVS and Blackboard MNIST will be released soon.



Table 1: Detection performance of YOLE.

	S-N-MNIST					S-MNIST-DVS	Blackboard MNIST	Poker-DVS	N-Caltech101
	v1	v2	v2*	v2fr	v2fr+ns				
accuracy	94.9	91.7	94.7	88.6	85.5	96.1	90.4	99.01	56.5
mAP	91.3	87.9	90.5	81.5	77.4	92.0	87.4	98.06	30.7

Table 2: Detection performance of eFCN.

	S-MNIST-DVS	Blackboard MNIST
accuracy	94.0	88.5
mAP	87.4	84.7

In all the experiments the first four convolutional layers have been initialized with kernels from a recognition network pretrained to classify MNIST-DVS digits, while the remaining layers have been initialized as proposed by Glorot and Bengio [8]. All networks were trained optimizing the multi-objective loss proposed by Redmon et al. [16] with Adam [17], learning rate  $10^{-4}$ ,  $\beta_1 = 0.9$ ,  $\beta_2 = 0.999$ ,  $\varepsilon = 10^{-8}$ . The batch size was chosen depending on the dataset: 10 for Shifted N-MNIST, 40 for Shifted MNIST-DVS and N-Caltech101, 25 for Blackboard MNIST and 35 for Poker-DVS with the aim of filling the memory of the GPU at best. Early-stopping was applied to prevent overfitting.

## 4.1 Results and Discussion

**Detection performance of YOLE.** The YOLE network achieves good detection results both in terms of mean average precision (mAP) [6] and accuracy (which in this case is computed by matching every ground truth bounding box with the predicted one having the highest IOU) in most of the datasets. The results we obtained are summarized in Table 1.

We used the Shifted N-MNIST dataset also to analyze how detection performance changes when the network is used to process scenes composed of a variable number of objects. We denote as  $v1$  the results obtained using scenes composed of a single digit, with  $v2$  those obtained with scenes containing two digits in random locations of the field of view. We further tested the robustness of the proposed model by adding some challenging noise, *i.e.*, higher than what can be usually experienced with event cameras. We added non-target objects ( $v2fr$ ) in the form of five  $8 \times 8$  fragments, taken from random N-MNIST digits using a procedure similar to the one used to build the *Cluttered Translated MNIST* dataset [18], and 200 additional random events per frame ( $v2fr+ns$ ). In case of multiple object the algorithm is still able to detect the all of them, while, as expected, performance drops both in terms of accuracy and mean average precision when dealing with noisy data. Nevertheless, we have very good detection performance on the Shifted MNIST-DVS, Blackboard MNIST and Poker-DVS datasets which represent a more realistic scenario in terms of noise.

All of these experiments were performed using the set of hyperparameters suggested by the original work from Redmon et al. [16]. However, a different choice of these parameters, namely  $\lambda_{coord} = 25.0$  and  $\lambda_{noobj} = 0.25$ , worked better for us increasing both the accuracy and mean average precision scores ( $v2^*$ ).

The dataset in which the proposed model did not achieve noticeable results is N-Caltech101. This is mainly explained by the fact that the number of samples in each class is not evenly balanced. The network, indeed, achieves good results as for those obtained in the other datasets when the number of training samples is high such as with *Airplanes*, *Motorbikes*



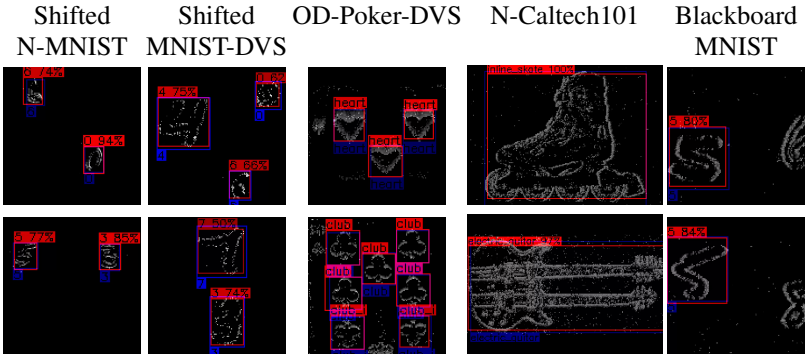


Figure 4: Examples of YOLE predictions.

and *Faces\_easy* (see Table 1 and Table 2 in the supplementary material). As the number of training samples decreases, however, the performance of the model becomes worse, behavior which explains the poor aggregate scores we report here in Table 1.

**Detection performance of eFCN.** We tested the performance of the eFCN network on two datasets: the Shifted MNIST-DVS and Blackboard MNIST datasets. With this fully-convolutional variant of the network we registered a slight decrease in performance w.r.t. the results we obtained using YOLE, as reported in Table 2. This gap in performance is mainly due to the fact that each region in eFCN generates its predictions by only looking at the visual information contained in its portion of the field of view. Indeed, if an object is only partially contained inside a region the network has to guess the object dimensions and class by only looking at a restricted region of the frame. However, removing the last fully-connected layers allowed us to design a detection network made of only event-based layers and which also uses a significantly lower number of parameters. In the supplementary materials we provide a video showing a comparison between the predictions obtained using the two proposed networks, YOLE and eFCN.

**Timing performance of the event-based framework.** In order to identify the advantages and weaknesses of our event-based framework we compared our detection networks on two datasets, Shifted N-MNIST and Blackboard MNIST. In the first one the event-based approach achieved a 2x speedup (22.6ms per frame), whereas in the second one it performed slightly slower (43.2ms per frame) w.r.t. a network using conventional layers (34.6ms per frame). The second benchmark is indeed challenging for our framework since changes are not localized in restricted regions of the frame due to the presence of noise and large objects covering multiple regions. In these conditions, where most of the feature maps need to be recalculated, a conventional frame-based approach performs better since it has not to deal with the overhead of additional event information.

## 5 Conclusions

In this paper we proposed two different methods, based on the YOLO architecture, to accomplish object detection in event-based cameras. The first one, namely YOLE, integrates events into a unique frame to make them usable with YOLO. Conversely, eFCN relies on a more general extension of the convolutional and max pooling layers to deal directly with events and to exploit their sparsity to avoid reprocessing the whole network. This novel

event-based framework can be used in every fully-convolutional architecture to make it usable with event-cameras, even conventional CNN for classification, although in this paper it has been applied to object detection networks.

We analyzed the timing performance of this formalization obtaining promising results. We are planning to extend our framework to automatically detect at runtime when the use of event-based layers speeds up computation (*i.e.*, changes affect few regions of the frame) or a complete recomputation of the feature maps is more beneficial in order to exploit the benefits of both approaches. Nevertheless, we believe that a hardware implementation, *e.g.*, with FPGAs, would allow to better exploit the advantages of the proposed method enabling a fair timing comparison with SNNs, which are usually implemented in hardware.

## References

- [1] Patrick Bardow, Andrew J Davison, and Stefan Leutenegger. Simultaneous optical flow and intensity estimation from an event camera. In *Proceedings of the IEEE Conference on Computer Vision and Pattern Recognition*, pages 884–892, 2016.
- [2] Raphael Berner, C Brandli, Minhao Yang, Shih-Chii Liu, and T Delbruck. A  $240 \times 180$  10mw 12us latency sparse-output vision sensor for mobile applications. pages C186–C187, 01 2013.
- [3] Blender Online Community. *Blender - a 3D modelling and rendering package*. Blender Foundation, Blender Institute, Amsterdam, 2017. URL <http://www.blender.org>.
- [4] Nicholas F. Y. Chen. Pseudo-labels for Supervised Learning on Dynamic Vision Sensor Data, Applied to Object Detection under Ego-motion. *arXiv*, Sep 2017. URL <https://arxiv.org/abs/1709.09323>.
- [5] Martin Ester, Hans-Peter Kriegel, Jörg Sander, and Xiaowei Xu. A density-based algorithm for discovering clusters a density-based algorithm for discovering clusters in large spatial databases with noise. In *Proceedings of the Second International Conference on Knowledge Discovery and Data Mining*, KDD’96, pages 226–231. AAAI Press, 1996. URL <http://dl.acm.org/citation.cfm?id=3001460.3001507>.
- [6] Mark Everingham, Luc Van Gool, Christopher K. I. Williams, John Winn, and Andrew Zisserman. The Pascal Visual Object Classes (VOC) Challenge. *Int. J. Comput. Vision*, 88(2):303–338, Jun 2010. ISSN 1573-1405. doi: 10.1007/s11263-009-0275-4.
- [7] Li Fei-Fei, R. Fergus, and P. Perona. One-shot learning of object categories. *IEEE Trans. Pattern Anal. Mach. Intell.*, 28(4):594–611, Apr 2006. ISSN 0162-8828. doi: 10.1109/TPAMI.2006.79.
- [8] Xavier Glorot and Yoshua Bengio. Understanding the difficulty of training deep feed-forward neural networks. *PMLR*, pages 249–256, Mar 2010. ISSN 1938-7228. URL <http://proceedings.mlr.press/v9/glorot10a.html>.
- [9] Kaiming He, Xiangyu Zhang, Shaoqing Ren, and Jian Sun. Deep residual learning for image recognition. In *Proceedings of the IEEE conference on computer vision and pattern recognition*, pages 770–778, 2016.

- [10] Diederik P. Kingma and Jimmy Ba. Adam: A Method for Stochastic Optimization. *arXiv*, Dec 2014. URL <https://arxiv.org/abs/1412.6980>.
- [11] Thomas N. Kipf and Max Welling. Semi-supervised classification with graph convolutional networks. In *International Conference on Learning Representations (ICLR)*, 2017.
- [12] Alex Krizhevsky, Ilya Sutskever, and Geoffrey E Hinton. Imagenet classification with deep convolutional neural networks. In F. Pereira, C. J. C. Burges, L. Bottou, and K. Q. Weinberger, editors, *Advances in Neural Information Processing Systems* 25, pages 1097–1105. Curran Associates, Inc., 2012. URL <http://papers.nips.cc/paper/4824-imagenet-classification-with-deep-convolutional-neural-pdf>.
- [13] Y. Lecun, L. Bottou, Y. Bengio, and P. Haffner. Gradient-based learning applied to document recognition. *Proc. IEEE*, 86(11):2278–2324, Nov 1998. ISSN 0018-9219. doi: 10.1109/5.726791.
- [14] J. Li, F. Shi, W. Liu, D. Zou, Q. Wang, H. Lee, P.-K. Park, and H. E. Ryu. Adaptive temporal pooling for object detection using dynamic vision sensor. *British Machine Vision Conference (BMVC)*, 2017.
- [15] Wei Liu, Dragomir Anguelov, Dumitru Erhan, Christian Szegedy, Scott Reed, Cheng-Yang Fu, and Alexander C Berg. Ssd: Single shot multibox detector. In *European conference on computer vision*, pages 21–37. Springer, 2016.
- [16] Jonathan Long, Evan Shelhamer, and Trevor Darrell. Fully convolutional networks for semantic segmentation. In *Proceedings of the IEEE conference on computer vision and pattern recognition*, pages 3431–3440, 2015.
- [17] Wolfgang Maass. Networks of spiking neurons: the third generation of neural network models. *Neural networks*, 10(9):1659–1671, 1997.
- [18] Volodymyr Mnih, Nicolas Heess, Alex Graves, et al. Recurrent models of visual attention. In *Advances in neural information processing systems*, pages 2204–2212, 2014.
- [19] Federico Monti, Davide Boscaini, Jonathan Masci, Emanuele Rodola, Jan Svoboda, and Michael M Bronstein. Geometric deep learning on graphs and manifolds using mixture model cnns. In *Proceedings of the IEEE Conference on Computer Vision and Pattern Recognition*, pages 5115–5124, 2017.
- [20] Elias Mueggler, Henri Rebecq, Guillermo Gallego, Tobi Delbruck, and Davide Scaramuzza. The Event-Camera Dataset and Simulator: Event-based Data for Pose Estimation, Visual Odometry, and SLAM. *arXiv*, Oct 2016. URL <https://arxiv.org/abs/1610.08336>.
- [21] Elias Mueggler, Chiara Bartolozzi, and Davide Scaramuzza. Fast event-based corner detection. In *British Machine Vision Conference (BMVC)*, number EPFL-CONF-232510, 2017.

- [22] Daniel Neil, Michael Pfeiffer, and Shih-Chii Liu. Phased lstm: Accelerating recurrent network training for long or event-based sequences. In *Advances in Neural Information Processing Systems*, pages 3882–3890, 2016.
- [23] G. Orchard, C. Meyer, R. Etienne-Cummings, C. Posch, N. Thakor, and R. Benosman. HFirst: A Temporal Approach to Object Recognition. *IEEE Trans. Pattern Anal. Mach. Intell.*, 37(10):2028–2040, Jan 2015. ISSN 0162-8828. doi: 10.1109/TPAMI.2015.2392947.
- [24] Garrick Orchard, Ajinkya Jayawant, Gregory K. Cohen, and Nitish Thakor. Converting Static Image Datasets to Spiking Neuromorphic Datasets Using Saccades. *Front. Neurosci.*, 9, Nov 2015. ISSN 1662-453X. doi: 10.3389/fnins.2015.00437.
- [25] José Antonio Pérez-Carrasco, Bo Zhao, Carmen Serrano, Begoña Acha, Teresa Serrano-Gotarredona, Shouchun Chen, and Bernabé Linares-Barranco. Mapping from frame-driven to frame-free event-driven vision systems by low-rate rate coding and coincidence processing—application to feedforward ConvNets. *IEEE Trans. Pattern Anal. Mach. Intell.*, 35(11):2706–2719, Nov 2013. ISSN 1939-3539. doi: 10.1109/TPAMI.2013.71.
- [26] C. Posch, D. Matolin, and R. Wohlgenannt. A QVGA 143 dB Dynamic Range Frame-Free PWM Image Sensor With Lossless Pixel-Level Video Compression and Time-Domain CDS. *IEEE J. Solid-State Circuits*, 46(1):259–275, Jan 2011. ISSN 0018-9200. doi: 10.1109/JSSC.2010.2085952.
- [27] Aman Raj, Daniel Maturana, and Sebastian Scherer. Multi-scale convolutional architecture for semantic segmentation. page 14, 01 2015.
- [28] Bharath Ramesh, Hong Yang, Garrick Orchard, Ngoc Anh Le Thi, and Cheng Xiang. DART: Distribution Aware Retinal Transform for Event-based Cameras. *arXiv*, Oct 2017. URL <https://arxiv.org/abs/1710.10800>.
- [29] Henri Rebecq, Timo Horstschaef, Guillermo Gallego, and Davide Scaramuzza. Evo: A geometric approach to event-based 6-dof parallel tracking and mapping in real time. *IEEE Robotics and Automation Letters*, 2(2):593–600, 2017.
- [30] Joseph Redmon, Santosh Divvala, Ross Girshick, and Ali Farhadi. You only look once: Unified, real-time object detection. In *Proceedings of the IEEE conference on computer vision and pattern recognition*, pages 779–788, 2016.
- [31] Shaoqing Ren, Kaiming He, Ross Girshick, and Jian Sun. Faster r-cnn: Towards real-time object detection with region proposal networks. In *Advances in neural information processing systems*, pages 91–99, 2015.
- [32] T. Serrano-Gotarredona and B. Linares-Barranco. A  $128 \times 128$  1.5 % Contrast Sensitivity 0.9 % FPN  $3 \mu\text{s}$  Latency 4 mW Asynchronous Frame-Free Dynamic Vision Sensor Using Transimpedance Preamplifiers. *IEEE J. Solid-State Circuits*, 48(3):827–838, Mar 2013. ISSN 0018-9200. doi: 10.1109/JSSC.2012.2230553.
- [33] Teresa Serrano-Gotarredona and Bernabé Linares-Barranco. Poker-DVS and MNIST-DVS. Their History, How They Were Made, and Other Details. *Front. Neurosci.*, 9, Dec 2015. ISSN 1662-453X. doi: 10.3389/fnins.2015.00481.

- [34] K. Simonyan and A. Zisserman. Very deep convolutional networks for large-scale image recognition. *CoRR*, abs/1409.1556, 2014.
- [35] Christian Szegedy, Sergey Ioffe, Vincent Vanhoucke, and Alexander A Alemi. Inception-v4, inception-resnet and the impact of residual connections on learning. In *AAAI*, volume 4, page 12, 2017.
- [36] Fisher Yu and Vladlen Koltun. Multi-Scale Context Aggregation by Dilated Convolutions. In *International Conference on Learning Representations (ICLR)*, 2016.
- [37] B. Zhao, R. Ding, S. Chen, B. Linares-Barranco, and H. Tang. Feedforward Categorization on AER Motion Events Using Cortex-Like Features in a Spiking Neural Network. *IEEE Trans. Neural Networks Learn. Syst.*, 26(9):1963–1978, Sep 2015. ISSN 2162-237X. doi: 10.1109/TNNLS.2014.2362542.

# Event-based Convolutional Networks for Object Detection in Neuromorphic Cameras

## Supplementary material

Marco Cannici  
marco.cannici@mail.polimi.it

Politecnico di Milano  
Milano, Italy

Marco Ciccone  
marco.ciccone@polimi.it

Andrea Romanoni  
andrea.romanoni@polimi.it

Matteo Matteucci  
matteo.matteucci@polimi.it

In this document we describe our novel event-based datasets adopted in the paper "Event-based Convolutional Network for Object Detection in Neuromorphic Cameras" and the object-specific detection performance in the N-Caltech101 dataset.

## 1 Event-based object detection datasets

Due to the lack of object detection datasets with event cameras, we extended the publicly available N-MNIST, MNIST-DVS, Poker-DVS and we propose a novel dataset based on MNIST, i.e., Blackboard MNIST. They will be soon released, however, in Figure 1 we reported some example from the four datasets.

### 1.1 Shifted N-MNIST

The original N-MNIST [24] extends the well-known MNIST [13]: it provides an event-based representation of both the full training set (60,000 samples) and the full testing set (10,000 samples) to evaluate object classification algorithms. The dataset has been recorded by means of event camera in front of an LCD screen and moved to detect static MNIST digits displayed on the monitor. For further details we refer the reader to [24].

Starting from the N-MNIST dataset, we built a more complex set of recordings that we used to train the object detection network to detect multiple objects in the same scene. We created two versions of the dataset, Shifted N-MNIST v1 and Shifted N-MNIST v2, that contains respectively one or two non overlapping  $34 \times 34$  N-MNIST digits per sample randomly positioned on a bigger surface. We used different surface dimensions in our tests which vary from double the original size,  $68 \times 68$ , up to  $124 \times 124$ . The dimension and structure of the resulting dataset is the same of the original N-MNIST collection.

To extend the dataset for object detection evaluation, the bounding boxes ground truth are required. To estimate them we first integrate events into a single frame as described in Section 2 of the original paper. We remove the noise by considering only non-zero pixels

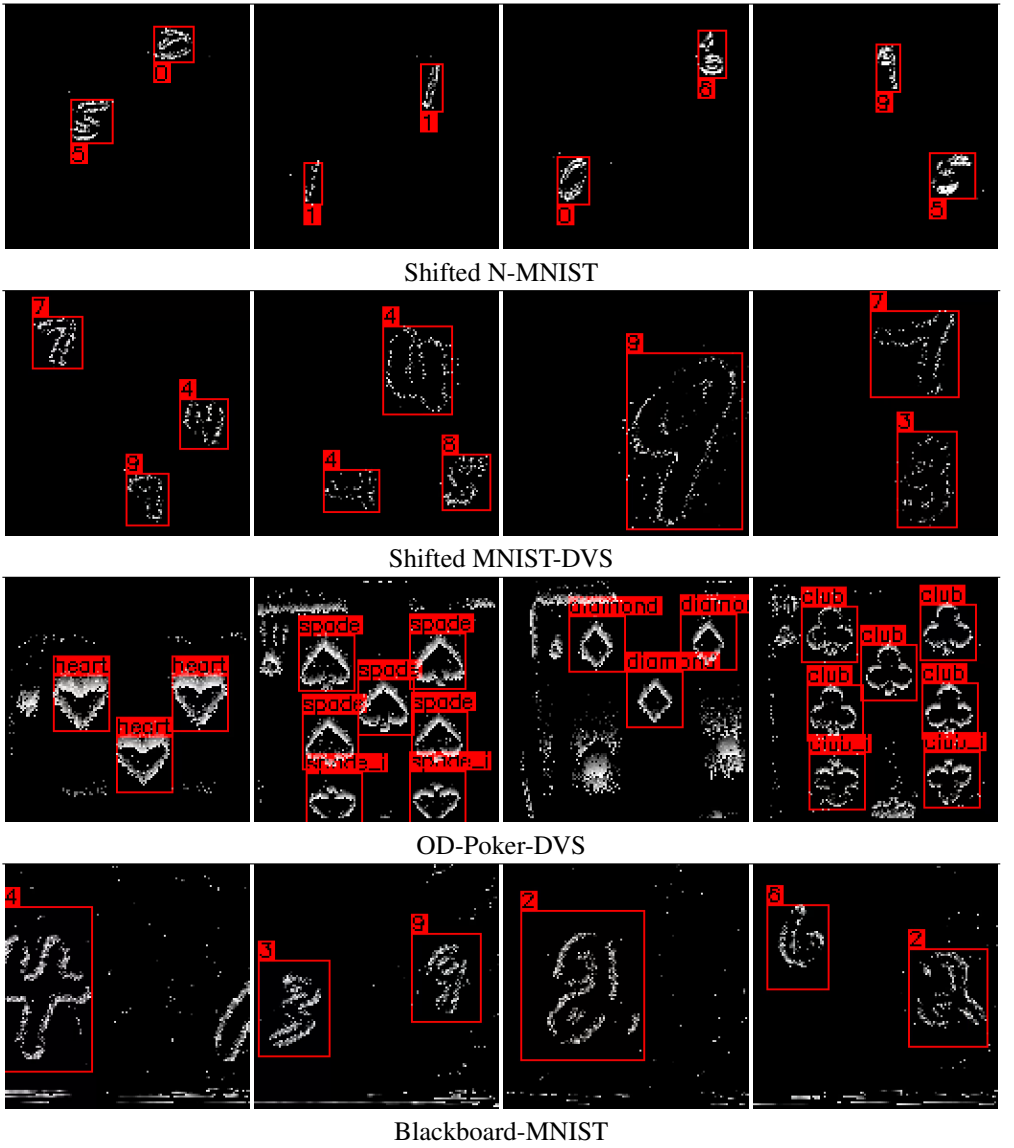


Figure 1: Examples of samples from the proposed dataset.

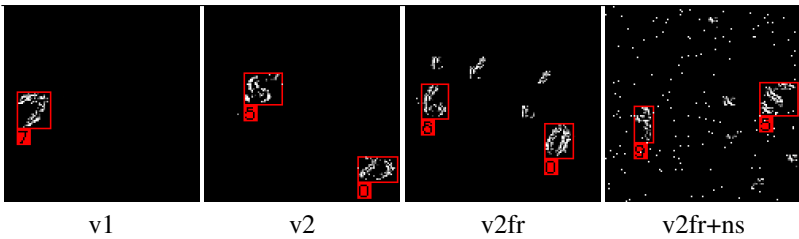


Figure 2: Different versions of Shifted N-MNIST.



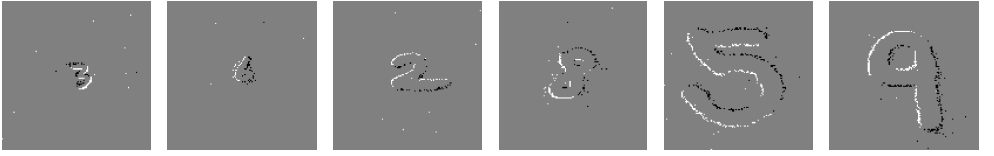


Figure 3: Examples of the three different scales of MNIST-DVS digits. Two samples at *scale4*, two at *scale8* and two at *scale16*.

having at least other  $\rho$  non-zero pixels around them within a circle of radius  $R$ . All the other pixels are considered noise. Then, with a custom version of the DBSCAN [15] density-based clustering algorithm we group pixels into a single cluster. A threshold  $min_{area}$  is used to filter out small bounding boxes extracted in correspondence of low events activities. This condition usually happens during the transition from a saccade to the next one as the camera remains still for a small fraction of time and no events are generated. We used  $\rho = 3$ ,  $R = 2$  and  $min_{area} = 10$ . The coordinates of these bounding boxes are then shifted based on the final position the digit has in the bigger field of view.

For each N-MNIST sample, another digit was randomly selected in the same portion of the dataset (training, testing or validation) to form a new example. The final dataset contains 60,000 training samples and 10,000 testing samples, as for the original N-MNIST dataset. In Figure 2 we illustrate one example for v1 and the three variants of v2 we adopted (and described) in the paper.

## 1.2 Shifted MNIST-DVS

The MNIST-DVS dataset [16] is another collection of event-based recordings that extends MNIST [17]. It consists of 30,000 samples recorded by displaying digits on a screen in front of a event camera, but differently from N-MNIST, they move digits on the screen instead of the sensors, and they use the digits at three different scales, i.e., *scale4*, *scale8* and *scale16*. The resulting dataset is composed of 30,000 event-based recordings showing each one of the selected 10,000 MNIST digits on three different dimensions. Examples of these recordings are shown in Figure 3.

We used MNIST-DVS recordings to build a detection dataset by means of a procedure similar to the one we used to create the Shifted N-MNIST dataset. However in this case we mix together digits of multiple scales. All the MNIST-DVS samples, despite of the actual dimensions of the digits being recorded, are contained within a fixed  $128 \times 128$  field of view. Digits are placed centered inside the scene and occupy a limited portion of the frame, especially those belonging to the smallest and middle scales. In order to place multiple examples on the same scene we first cropped the three scales of samples into smaller recordings occupying  $35 \times 35$ ,  $65 \times 65$  and  $105 \times 105$  spatial regions respectively. The bounding boxes annotations and the final examples were obtained by means of the same procedure we used to construct the Shifted N-MNIST dataset. These recordings were built by mixing digits of different dimensions in the same sample. Based on the original samples dimensions, we decided to use the following four configurations (which specify the number of samples of each category used to build a single Shifted MNIST-DVS example): (i) three *scale4* digits, (ii) two *scale8* digits, (iii) two *scale4* digits mixed with one *scale8* digit (iv) one *scale16* digit placed in random locations of the field of view. The overall dataset is composed of 30,000

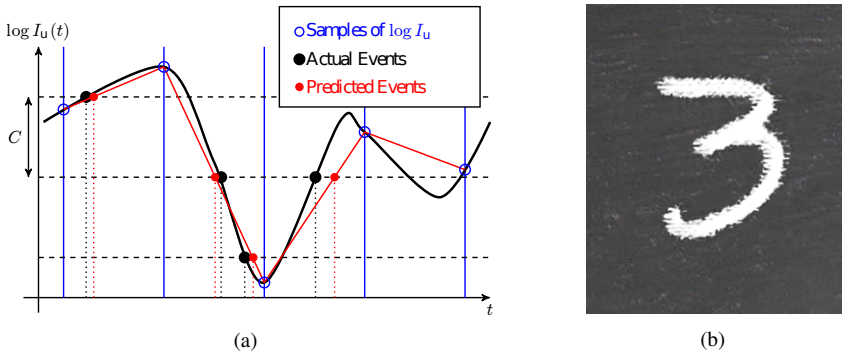


Figure 4: (a) The image shows in black the intensity, expressed as  $\log I_u(t)$ , of a single pixel  $\mathbf{u} = (x, y)$ . This curve is sampled at a constant rate when frames are generated by Blender, shown in figure as vertical blue lines. The sampled values thus obtained (blue circles) are used to approximate the pixel intensity by means of a simple piecewise linear time interpolation (red line). Whenever this curve crosses one of the threshold values (horizontal dashed lines) a new event is generated with the corresponding predicted timestamp. (Figure from [14]) (b) A preprocessed MNIST digit on top of the blackboard’s background.

samples containing these four possible configurations.

### 1.3 OD-Poker-DVS

The original Poker-DVS [14] have been proposed to test object recognition algorithms; it is a small collection of neuromorphic recordings obtained by quickly browsing custom made poker card decks in front of a DVS camera for 2-4 seconds. The dataset is composed of 131 samples containing centered pips of the four possible categories (spades, hearts, diamonds or clubs) extracted from three decks recordings. Single pips were extracted by means of an event-based tracking algorithms which was used to follow symbols inside the scene and to extract  $31 \times 31$  pixels examples.

With OD-Poker-DVS we extend its scope to test also object detection. To do so we used the event-based tracking algorithm provided with the original dataset to follow the movement of the  $31 \times 31$  samples in the uncut recordings and extract their bounding boxes.

Even if composed of a limited amount of samples, this dataset represents an interesting real-world application that highlights the potential of event-based vision sensors. The nature of the data acquisition is indeed particularly well suited to neuromorphic cameras due to their very high temporal resolution. Symbols are clearly visible inside the recordings even if they move at very high speed. Each pip, indeed, takes from 10 to 30 ms to cross the screen but it can be easily recognized within the first 1-2 ms.

### 1.4 MNIST Blackboard

The two dataset based on MNIST presented in Section 1.1 and 1.2 have the drawback of recording digits at predefined sizes. Therefore, in Blackboard MNIST we propose a more challenging scenario that consists of a number of samples showing digits (from the original MNIST dataset) written on a blackboard in random positions and with different scales.

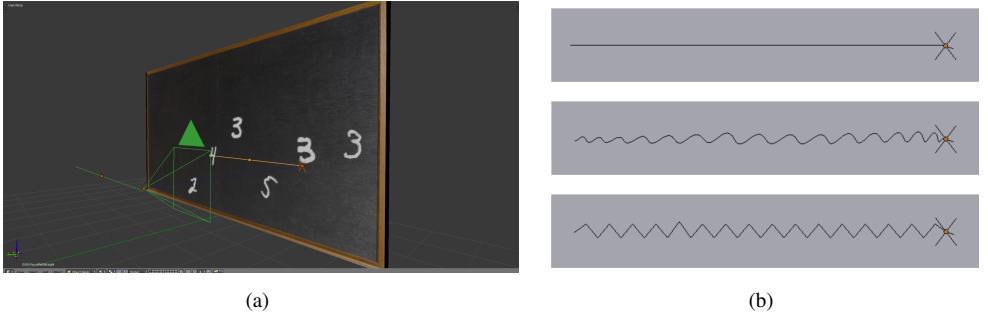


Figure 5: **(a)** The 3D scene used to generate the Blackboard MNIST dataset. The camera moves in front of the blackboard along a straight trajectory while following a *focus object* that moves on the blackboard’s surface, synchronized with the camera. The camera and its trajectory are depicted in green, the focus object is represented as a red cross and, finally, its trajectory is depicted as a yellow line. **(b)** The three types of focus trajectories.

We used the DAVIS simulator released by [24] to build our own set of synthetic recordings. Given a three-dimensional virtual scene and the trajectory of a moving camera within it, the simulator is able to generate a stream of events describing the visual information captured by the virtual camera. The system uses Blender [9], an open-source 3D modeling tool, to generate thousands of rendered frames along a predefined camera trajectory which are then used to reconstruct the corresponding neuromorphic recording. The intensity value of each single pixel inside the sequence of rendered frames, captured at a constant frame-rate, is tracked. As Figure 4(a) shows, an event is generated whenever the log-intensity of a pixel crosses an intensity threshold, as in a real event-based camera. A piecewise linear time interpolation mechanism is used to determine brightness changes in the time between frames in order to simulate the microseconds timestamp resolution of a real sensor. We extended the simulator to output bounding boxes annotations associated to every visible digit.

We used Blender APIs to place MNIST digits in random locations of a blackboard and to record their position with respect to the camera point of view. Original MNIST images depict black handwritten digits on a white background. To mimic the chalk on the blackboard, we removed the background, we turned digits in white and we roughen their contours to make them look like if their were written with a chalk. An example is shown in Figure 4(b).

The scene contains the image of a blackboard on a vertical plane and a virtual camera with  $128 \times 128$  resolution that moves horizontally on a predefined trajectory parallel to the blackboard plane (see Figure 5(a)). The camera points a hidden object that moves on the blackboard surface, synchronized with the camera, following a given trajectory. To introduce variability in the camera movement, and to allow all the digits outline to be seen (and possibly detected), we used different trajectories that vary from a straight path to a smooth or triangular undulating path that makes the camera tilt along the transverse axis while moving (Figure 5(b)).

Before starting the simulation, we randomly select a number of preprocessed MNIST digits and place them in a random portion of the blackboard. The camera moves so that all the digits will be framed during the camera movement. The simulation is then finally started on this modified scene to generate neuromorphic recordings. Every time a frame is rendered during the simulation, the bounding boxes of all the visible digits inside the frame

are also extracted. This operation is performed by computing the camera space coordinates (or normalized device coordinates) of the top-left and bottom-right vertex of all the images inside the field of view. Since images are slightly larger than the actual digits they contain, we manually cropped every bounding box to better enclose each digit and also to compensate the small offset in the pixels position introduced by the camera motion and by the linear interpolation mechanism. In addition, bounding boxes corresponding to objects which are only partially visible are also filtered out. In order to build the final detection dataset, this generation process is executed multiple times, each time with different digits.

We built three sub-collections of recordings with increasing level of complexity which we merged together to obtain our final dataset: *Blackboard MNIST EASY*, *Blackboard MNIST MEDIUM*, *Blackboard MNIST HARD*. In *Blackboard MNIST EASY*, we used digits of only one dimension (roughly corresponding to the middle scale of MNIST-DVS samples) and a single type of camera trajectory which moves the camera from right to left with the focus object moving in a straight line. In addition, only three objects were placed on the blackboard using only a fixed portion of its surface. We collected a total of 1,200 samples (1,000 training, 100 testing, 100 validation).

*Blackboard MNIST MEDIUM* features more variability in the number and dimensions of the digits and in the types of camera movements. Moreover, the portion of the blackboard on which digits were added varies and may cover any region of the blackboard, even those near its edges. The camera motions were also extended to the set of all possible trajectories that combine either left-to-right or right-to-left movements with variable paths of the focus object. We used three types of trajectories for this object: a straight line, a triangular path or a smooth curved trajectory, all parallel to the camera trajectory and placed around the position of the digits on the blackboard. One of these path was selected randomly for every generated sample. Triangular and curved trajectories were introduced as we noticed that sudden movements of the camera produce burst of events that we wanted our detection system to be able to handle. The number and dimensions of the digits were chosen following three possible configurations, similarly to the Shift MNIST-DVS dataset: either six small digits (with sizes comparable to *scale4* MNIST-DVS digits), three intermediate-size digits (comparable to the MNIST-DVS *scale8*) or two big digits (comparable to the biggest scale of the MNIST-DVS dataset, *scale16*). A set of 1,200 recordings was generated using the same splits of the first variant and with equal amount of samples in each one of the three configurations.

Finally, *Blackboard MNIST HARD* contains digits recorded by using the second and third configuration of objects we described previously. However, in this case each image was resized to a variable size spanning from the original configuration size down to the previous scale. A total of 600 new samples (500 training, 50 testing, 50 validation) were generated, 300 of them containing three digits each and the remaining 300 consisting of two digits with variable size.

The three collections can be used individually or jointly; the whole *Blackboard MNIST* dataset contains 3,000 samples in total (2500 training, 250 testing, 250 validation). Examples of different objects configurations are shown in Figure 6. Samples were saved by means of the AEDAT v3.1 file format for event-based recordings.

## 2 Results

In the video attachment we illustrate the detection results of YOLE and eFCN.

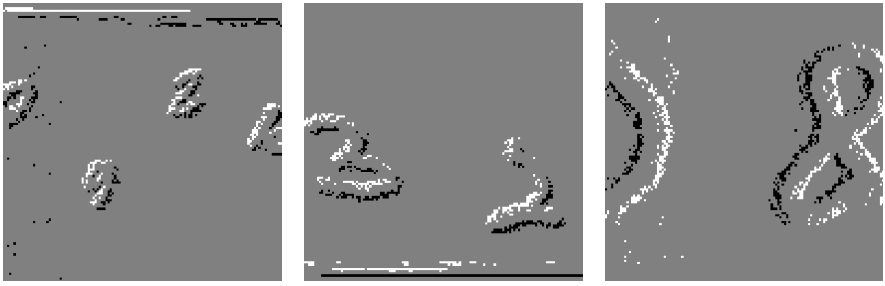


Figure 6: Examples of the three types of objects configurations used to generate the second collection of the Blackboard MNIST dataset.

Table 3 and Table 4 provide a detailed analysis of the model performance on some N-Caltech101 categories.

## References

- [1] Patrick Bardow, Andrew J Davison, and Stefan Leutenegger. Simultaneous optical flow and intensity estimation from an event camera. In *Proceedings of the IEEE Conference on Computer Vision and Pattern Recognition*, pages 884–892, 2016.
- [2] Raphael Berner, C Brandli, Minhao Yang, Shih-Chii Liu, and T Delbruck. A  $240 \times 180$  10mw 12us latency sparse-output vision sensor for mobile applications. pages C186–C187, 01 2013.
- [3] Blender Online Community. *Blender - a 3D modelling and rendering package*. Blender Foundation, Blender Institute, Amsterdam, 2017. URL <http://www.blender.org>.
- [4] Nicholas F. Y. Chen. Pseudo-labels for Supervised Learning on Dynamic Vision Sensor Data, Applied to Object Detection under Ego-motion. *arXiv*, Sep 2017. URL <https://arxiv.org/abs/1709.09323>.
- [5] Martin Ester, Hans-Peter Kriegel, Jörg Sander, and Xiaowei Xu. A density-based algorithm for discovering clusters a density-based algorithm for discovering clusters in large spatial databases with noise. In *Proceedings of the Second International Conference on Knowledge Discovery and Data Mining, KDD’96*, pages 226–231. AAAI Press, 1996. URL <http://dl.acm.org/citation.cfm?id=3001460.3001507>.
- [6] Mark Everingham, Luc Van Gool, Christopher K. I. Williams, John Winn, and Andrew Zisserman. The Pascal Visual Object Classes (VOC) Challenge. *Int. J. Comput. Vision*, 88(2):303–338, Jun 2010. ISSN 1573-1405. doi: 10.1007/s11263-009-0275-4.
- [7] Li Fei-Fei, R. Fergus, and P. Perona. One-shot learning of object categories. *IEEE Trans. Pattern Anal. Mach. Intell.*, 28(4):594–611, Apr 2006. ISSN 0162-8828. doi: 10.1109/TPAMI.2006.79.

- [8] Xavier Glorot and Yoshua Bengio. Understanding the difficulty of training deep feed-forward neural networks. *PMLR*, pages 249–256, Mar 2010. ISSN 1938-7228. URL <http://proceedings.mlr.press/v9/glorot10a.html>.
- [9] Kaiming He, Xiangyu Zhang, Shaoqing Ren, and Jian Sun. Deep residual learning for image recognition. In *Proceedings of the IEEE conference on computer vision and pattern recognition*, pages 770–778, 2016.
- [10] Diederik P. Kingma and Jimmy Ba. Adam: A Method for Stochastic Optimization. *arXiv*, Dec 2014. URL <https://arxiv.org/abs/1412.6980>.
- [11] Thomas N. Kipf and Max Welling. Semi-supervised classification with graph convolutional networks. In *International Conference on Learning Representations (ICLR)*, 2017.
- [12] Alex Krizhevsky, Ilya Sutskever, and Geoffrey E Hinton. Imagenet classification with deep convolutional neural networks. In F. Pereira, C. J. C. Burges, L. Bottou, and K. Q. Weinberger, editors, *Advances in Neural Information Processing Systems 25*, pages 1097–1105. Curran Associates, Inc., 2012. URL <http://papers.nips.cc/paper/4824-imagenet-classification-with-deep-convolutional-neural-networks.pdf>.
- [13] Y. Lecun, L. Bottou, Y. Bengio, and P. Haffner. Gradient-based learning applied to document recognition. *Proc. IEEE*, 86(11):2278–2324, Nov 1998. ISSN 0018-9219. doi: 10.1109/5.726791.
- [14] J. Li, F. Shi, W. Liu, D. Zou, Q. Wang, H. Lee, P.-K. Park, and H. E. Ryu. Adaptive temporal pooling for object detection using dynamic vision sensor. *British Machine Vision Conference (BMVC)*, 2017.
- [15] Wei Liu, Dragomir Anguelov, Dumitru Erhan, Christian Szegedy, Scott Reed, Cheng-Yang Fu, and Alexander C Berg. Ssd: Single shot multibox detector. In *European conference on computer vision*, pages 21–37. Springer, 2016.
- [16] Jonathan Long, Evan Shelhamer, and Trevor Darrell. Fully convolutional networks for semantic segmentation. In *Proceedings of the IEEE conference on computer vision and pattern recognition*, pages 3431–3440, 2015.
- [17] Wolfgang Maass. Networks of spiking neurons: the third generation of neural network models. *Neural networks*, 10(9):1659–1671, 1997.
- [18] Volodymyr Mnih, Nicolas Heess, Alex Graves, et al. Recurrent models of visual attention. In *Advances in neural information processing systems*, pages 2204–2212, 2014.
- [19] Federico Monti, Davide Boscaini, Jonathan Masci, Emanuele Rodola, Jan Svoboda, and Michael M Bronstein. Geometric deep learning on graphs and manifolds using mixture model cnns. In *Proceedings of the IEEE Conference on Computer Vision and Pattern Recognition*, pages 5115–5124, 2017.

- [20] Elias Mueggler, Henri Rebecq, Guillermo Gallego, Tobi Delbruck, and Davide Scaramuzza. The Event-Camera Dataset and Simulator: Event-based Data for Pose Estimation, Visual Odometry, and SLAM. *arXiv*, Oct 2016. URL <https://arxiv.org/abs/1610.08336>.
- [21] Elias Mueggler, Chiara Bartolozzi, and Davide Scaramuzza. Fast event-based corner detection. In *British Machine Vision Conference (BMVC)*, number EPFL-CONF-232510, 2017.
- [22] Daniel Neil, Michael Pfeiffer, and Shih-Chii Liu. Phased lstm: Accelerating recurrent network training for long or event-based sequences. In *Advances in Neural Information Processing Systems*, pages 3882–3890, 2016.
- [23] G. Orchard, C. Meyer, R. Etienne-Cummings, C. Posch, N. Thakor, and R. Benosman. HFirst: A Temporal Approach to Object Recognition. *IEEE Trans. Pattern Anal. Mach. Intell.*, 37(10):2028–2040, Jan 2015. ISSN 0162-8828. doi: 10.1109/TPAMI.2015.2392947.
- [24] Garrick Orchard, Ajinkya Jayawant, Gregory K. Cohen, and Nitish Thakor. Converting Static Image Datasets to Spiking Neuromorphic Datasets Using Saccades. *Front. Neurosci.*, 9, Nov 2015. ISSN 1662-453X. doi: 10.3389/fnins.2015.00437.
- [25] José Antonio Pérez-Carrasco, Bo Zhao, Carmen Serrano, Begoña Acha, Teresa Serrano-Gotarredona, Shouchun Chen, and Bernabé Linares-Barranco. Mapping from frame-driven to frame-free event-driven vision systems by low-rate rate coding and coincidence processing—application to feedforward ConvNets. *IEEE Trans. Pattern Anal. Mach. Intell.*, 35(11):2706–2719, Nov 2013. ISSN 1939-3539. doi: 10.1109/TPAMI.2013.71.
- [26] C. Posch, D. Matolin, and R. Wohlgenannt. A QVGA 143 dB Dynamic Range Frame-Free PWM Image Sensor With Lossless Pixel-Level Video Compression and Time-Domain CDS. *IEEE J. Solid-State Circuits*, 46(1):259–275, Jan 2011. ISSN 0018-9200. doi: 10.1109/JSSC.2010.2085952.
- [27] Aman Raj, Daniel Maturana, and Sebastian Scherer. Multi-scale convolutional architecture for semantic segmentation. page 14, 01 2015.
- [28] Bharath Ramesh, Hong Yang, Garrick Orchard, Ngoc Anh Le Thi, and Cheng Xiang. DART: Distribution Aware Retinal Transform for Event-based Cameras. *arXiv*, Oct 2017. URL <https://arxiv.org/abs/1710.10800>.
- [29] Henri Rebecq, Timo Horstschaefer, Guillermo Gallego, and Davide Scaramuzza. Evo: A geometric approach to event-based 6-dof parallel tracking and mapping in real time. *IEEE Robotics and Automation Letters*, 2(2):593–600, 2017.
- [30] Joseph Redmon, Santosh Divvala, Ross Girshick, and Ali Farhadi. You only look once: Unified, real-time object detection. In *Proceedings of the IEEE conference on computer vision and pattern recognition*, pages 779–788, 2016.
- [31] Shaoqing Ren, Kaiming He, Ross Girshick, and Jian Sun. Faster r-cnn: Towards real-time object detection with region proposal networks. In *Advances in neural information processing systems*, pages 91–99, 2015.



- [32] T. Serrano-Gotarredona and B. Linares-Barranco. A  $128 \times 128$  1.5 % Contrast Sensitivity 0.9 % FPN  $3 \mu\text{s}$  Latency 4 mW Asynchronous Frame-Free Dynamic Vision Sensor Using Transimpedance Preamplifiers. *IEEE J. Solid-State Circuits*, 48(3):827–838, Mar 2013. ISSN 0018-9200. doi: 10.1109/JSSC.2012.2230553.
- [33] Teresa Serrano-Gotarredona and Bernabé Linares-Barranco. Poker-DVS and MNIST-DVS. Their History, How They Were Made, and Other Details. *Front. Neurosci.*, 9, Dec 2015. ISSN 1662-453X. doi: 10.3389/fnins.2015.00481.
- [34] K. Simonyan and A. Zisserman. Very deep convolutional networks for large-scale image recognition. *CoRR*, abs/1409.1556, 2014.
- [35] Christian Szegedy, Sergey Ioffe, Vincent Vanhoucke, and Alexander A Alemi. Inception-v4, inception-resnet and the impact of residual connections on learning. In *AAAI*, volume 4, page 12, 2017.
- [36] Fisher Yu and Vladlen Koltun. Multi-Scale Context Aggregation by Dilated Convolutions. In *International Conference on Learning Representations (ICLR)*, 2016.
- [37] B. Zhao, R. Ding, S. Chen, B. Linares-Barranco, and H. Tang. Feedforward Categorization on AER Motion Events Using Cortex-Like Features in a Spiking Neural Network. *IEEE Trans. Neural Networks Learn. Syst.*, 26(9):1963–1978, Sep 2015. ISSN 2162-237X. doi: 10.1109/TNNLS.2014.2362542.

Table 3: Top-20 average precisions on N-Caltech101.

	airplanes	Motorbikes	Faces_easy	inline_skate	minaret	dollar_bill	grand_piano	watch	laptop	menorah	Yin-yang	windsor_chair	soccer_ball	stapler	trilobite	stop_sign	accordion	cellphone	metronome	umbrella
AP	93.17	92.31	87.15	78.03	76.95	76.58	76.09	71.49	68.42	67.39	66.23	64.12	62.69	59.08	58.95	57.95	57.18	56.70	56.32	54.90
samples	480	480	261	19	46	32	61	145	49	53	36	34	40	27	52	40	33	37	20	45

Table 4: Worst-20 average precisions on N-Caltech101.

	kangaroo	beaver	lobster	crocodile_head	ant	flamingo	gerenuk	scorpion	elephant	llama	crayfish	ibis	panda	emu	mayfly	bass	crocodile	cannon	binocular	wild_cat
AP	6.15	5.61	5.36	5.03	4.96	4.35	4.32	4.19	3.89	3.64	3.09	3.02	2.84	1.43	1.20	0.82	0.22	0.08	0.00	0.00
samples	52	28	25	31	66	68	22	52	40	48	42	48	24	33	24	34	61	27	21	22